





Crater depth prediction in granular collisions: A uniaxial compression modelF. Corrales-Machín ^{1,*} Y. Nahmad-Molinari ^{1,†} G. Viera-López ² and R. Bartali ¹¹*Universidad Autónoma de San Luis Potosí, Instituto de Física, Avenida Parque Chapultepec 1570, San Luis Potosí 78295, México*²*Gran Sasso Science Institute, Viale Francesco Crispi 7, L'Aquila 67100, Italy*

(Received 7 November 2023; revised 23 February 2024; accepted 18 April 2024; published 28 May 2024)

Impact crater experiments in granular media traditionally involve loosely packed sand targets. However, this study investigates granular impact craters on both loosely and more tightly packed sand targets. We report experiments that consistently adhere to power-law scaling laws for diameter as a function of impacting energy, similar to those reported by other groups for their experiments utilizing both solid and granular projectiles. In contrast, we observe significant deviations in the depth versus energy power law predicted by previous models. To address this discrepancy, we introduce a physical model of uniaxial compression that explains how depth saturates in granular collisions. Furthermore, we present an energy balance alongside this model that describes the energy transfer mechanisms acting during crater formation. We found a better way to transfer vertical momentum to horizontal degrees of freedom as the impact surface compacts, resulting in shallow craters on compacted sandbox targets. Our results reveal depth-to-diameter aspect ratios from approximately 0.051 to 0.094, allowing us to interpret the shallowness of planetary craters at the light of the uniaxial compression mechanism proposed in this work.

DOI: [10.1103/PhysRevE.109.054907](https://doi.org/10.1103/PhysRevE.109.054907)**I. INTRODUCTION**

Remarkable visual phenomena resulting from the impact of solid or liquid objects on liquid surfaces [1], such as the transient corona-shaped splashes followed by undulating gravity waves, have long captivated observers. These captivating moments were unveiled through high-speed photographic techniques pioneered by Edgerton at MIT [2] (for stunning examples, visit website [2]). Conversely, when such impacts occur on the surfaces of solid materials, whether consolidated like granite or unconsolidated like sand, and when the energy involved is sufficiently high, they leave a lasting mark as an indelible scar [3,4]. This enduring impact, initiated by shock wave propagation and followed by the settling of ejecta, is a fundamental process in the formation and development of celestial bodies, including asteroids, planetesimals, and rocky planets [5]. It is a process that shapes planetary surfaces prior to or in conjunction with other geophysical forces such as erosional processes driven by wind and water, radiative heating and cooling (weathering), volcanic activity, and even plate tectonics.

The historical debate concerning the origins of craters, first observed on the Moon's surface by Galileo, was conclusively resolved during the latter half of the 20th century, thanks to the renewed interest spurred by the Apollo missions and the pioneering work of Melosh [6]. Nevertheless, since Gilbert's experiments in 1893 [7], wherein solid projectiles impacted

the surface of sand to model crater formation, questions have lingered regarding the relevance and suitability of these analog models. The primary challenge lies in reconciling the high speeds and energies inherent in planetary crater-forming collisions with the limitations of laboratory experiments, resulting in incomplete or partially overlapping ranges of their corresponding dimensionless scaling parameters.

One aspect of particular interest involves investigating how the packing density of fragile or loosely consolidated granular projectiles influences the ultimate morphological features of resultant craters. This research has yielded intriguing findings, including the formation of central peaks, sometimes accompanied by splashing jets for ultra-loose-packed targets [8,9].

However, it is not merely a matter of having equal dimensionless scaling numbers (such as the ratio of gravitational to dynamic pressures, described by the Froude number: $Fr = gd/2v^2$); it is equally crucial to replicate the same scaling laws observed in planetary objects during terrestrial experiments. Each type of experiment, whether involving explosions, hypervelocity impacts, or low-energy scenarios, exhibits its distinct signature in the scaling laws that describe its morphology.

Nahmad and colleagues [10] have highlighted both the differences and similarities in the scaling laws governing the morphological features of craters in planetary and laboratory settings. They observed that hypervelocity impacts, explosions, and solid objects penetrating loosely packed sand form craters with different power-law relationships for aspect ratios (volume vs diameter) compared to craters formed by impacts of fragile projectiles or those observed on celestial bodies such as the Moon, Ganymede, and Callisto.

Their findings have raised questions about the role played by the relative strength and packing between the target and

* Also at Universidad Autónoma de San Luis Potosí, Instituto de Física, Avenida Parque Chapultepec 1570, San Luis Potosí 78295, México; frankcm.work@gmail.com

† yuri@ifisica.uaslp.mx

the projectile, which is a central focus of our present study. Furthermore, their observations have revealed that as impact energy increases, the depth of craters saturates, but it is still an open problem for solid or granular impacts on tightly packed targets or the underlying physical mechanisms of saturation of depth which remain unexplained. In this context, our experiments aim to systematically investigate and comprehend how target material strength and compaction influence the final morphology of craters.

By proposing a Heckel's uniaxial compaction mechanism, where the compressibility of the target is proportional to its porosity, we model the impact and deposition of the projectile onto the target surface. This model enables us to accurately describe the compressive subsidence of the crater's floor caused by the dynamic pressure exerted by the impacting projectile.

II. EXPERIMENTAL SETUP

We constructed a square-based sandbox with dimensions of 45 cm per side and 15 cm in height as the surface or granular bed in which the crater forms after the impact of a sand lump projectile. Sand grains with a diameter of $d \leq 1.0$ mm, obtained by sieving, were deposited inside the box as the granular medium. Two equally prepared series of fragile projectiles were dropped off at different heights, ranging from 0.1 up to 20 m, in free fall. After conducting 15 dropping experiments from a 20 m height, a final velocity of 18.55 ± 1.23 m/s was measured, demonstrating good reproducibility. This results in a deviation of less than 5.67% from the theoretically calculated final speed of 19.78 m/s in this worst-case scenario. For smaller dropping heights, the error due to air drag is reduced. They impacted the free surface of a sandbox filled with loose or compacted sand in order to explore the influence of a more consolidated terrain on the crater formation mechanism and the final morphological features of the resulting craters.

The projectiles were prepared by compacting a mixture of wet sand (250 g of sand plus 47.5 ml of water) with 5.0 g of Portland cement (Portland Type II Compound CPC 30R RS, Cemento Cruz Azul) as an adhesive, constituting only 2% of the total weight. This blend was introduced into a spherical mold. The resulting projectiles are weakly consolidated granular spheres, exhibiting a diameter of 7.07 cm, a mass of 242.51 g, a density of $\rho = 1.31$ g/cm³, and a packing fraction of $\phi = 0.50$. Subsequently, the projectiles were allowed to dry at room temperature for one week. Finally, post drying, their yield strength was measured, denoted by $\sigma = 17.15 \pm 2.2$ kPa.

The sand utilized on the impact surface is the same material from which the granular projectiles were crafted. The density of solid silica is $\rho_g = 2.65$ g/cm³, and the angle of repose fluctuates between 40° and 44°. Decompaction of the sandbox target was accomplished by uniformly raking the granular medium inside the sandbox. To facilitate compaction, an additional 3.5 kg of sand was added to the sandbox, and a uniform pressure of approximately 1.0 kgf/cm² was applied to the surface by a mass of 92 kg placed on top of a cover lid of the sandbox. Consequently, the target attained a density for

loosely packed sand, $\rho_L = 1.39$ g/cm³, while the compacted target reached a density of $\rho_C = 1.52$ g/cm³.

After each collision event, a topographical map of the resulting crater's surface was obtained using a time of flight (ToF) camera (Microsoft Kinect One model 74Z-00001) positioned at a height of 102.7 cm perpendicular and stationary to the impact surface. At this working height, a resolution of 2.8025 mm/px is achieved in the X, Y plane, with ± 1 mm accuracy in the vertical axis. The Kinect camera was calibrated, resulting in a measurement error, for the two-dimensional plane, of ± 0.16 px with respect to the field of view of the infrared camera of 512×424 px.

Subsequently, the morphological characteristics of the formed crater are automatically detected and quantified using the PYTHON library CRATERSLAB [11], specifically designed for such purposes and offering morphometric features of experimental and planetary impact craters in an automated way [12]. The quantified features, plotted as functions of the impact energy, encompass parameters such as crater depth, major and minor diameters, central peak height, as well as the volumes of both the crater cavity and the material deposited above the original surface level.

III. RESULTS AND DISCUSSION

In Fig. 1, subsequent pictures of the crater formed by the impact of sand lumplike projectiles are presented. The first row in this figure depicts a loosely packed sand target, while the second row shows the case of a compacted sand target. In both scenarios, as the energy increases, the projectiles crumble into smaller pieces, excavating a larger and deeper crater.

The sequence of craters formed for increasing energy in a loosely packed target, as shown at the beginning in Fig. 1, clearly illustrates the crater formation process driven by the displacement volume of the target material due to the partial penetration of the intact projectile for low energies (note the deeper craters before fragmentation than immediately after). As the dropping height gradually increases, the crater diameter grows and, simultaneously, the projectile breaks down into smaller fragments, progressively filling the crater's bottom. With a further increase in collision energy, the diameter continues to enlarge, leading to the formation of a central peak or dome and ejecting more (and smaller) projectile fragments out of the crater's rim. Below each picture, a transversal section provided by the CRATERSLAB library is shown to give a visual idea of the crater morphology. Only lateral dimension scales are different, while the vertical scale remains the same for all craters presented, showing the nonmonotonic trend of depth as a function of energy due to the transition that occurs when the projectile breaks apart.

In contrast, for the compacted target terrain, as illustrated in the second row of Fig. 1, the sequence initiates with the projectile breaking apart at lower dropping heights, resulting in an absence of noticeable crater excavation at low energies. The lower section of the projectile, which experiences the majority of the impact, is pulverized and remains confined on top of the target's terrain due to the dynamic pressure exerted by the avalanche of larger projectile fragments [8,13]. The confined pulverized portion of the projectile forms a

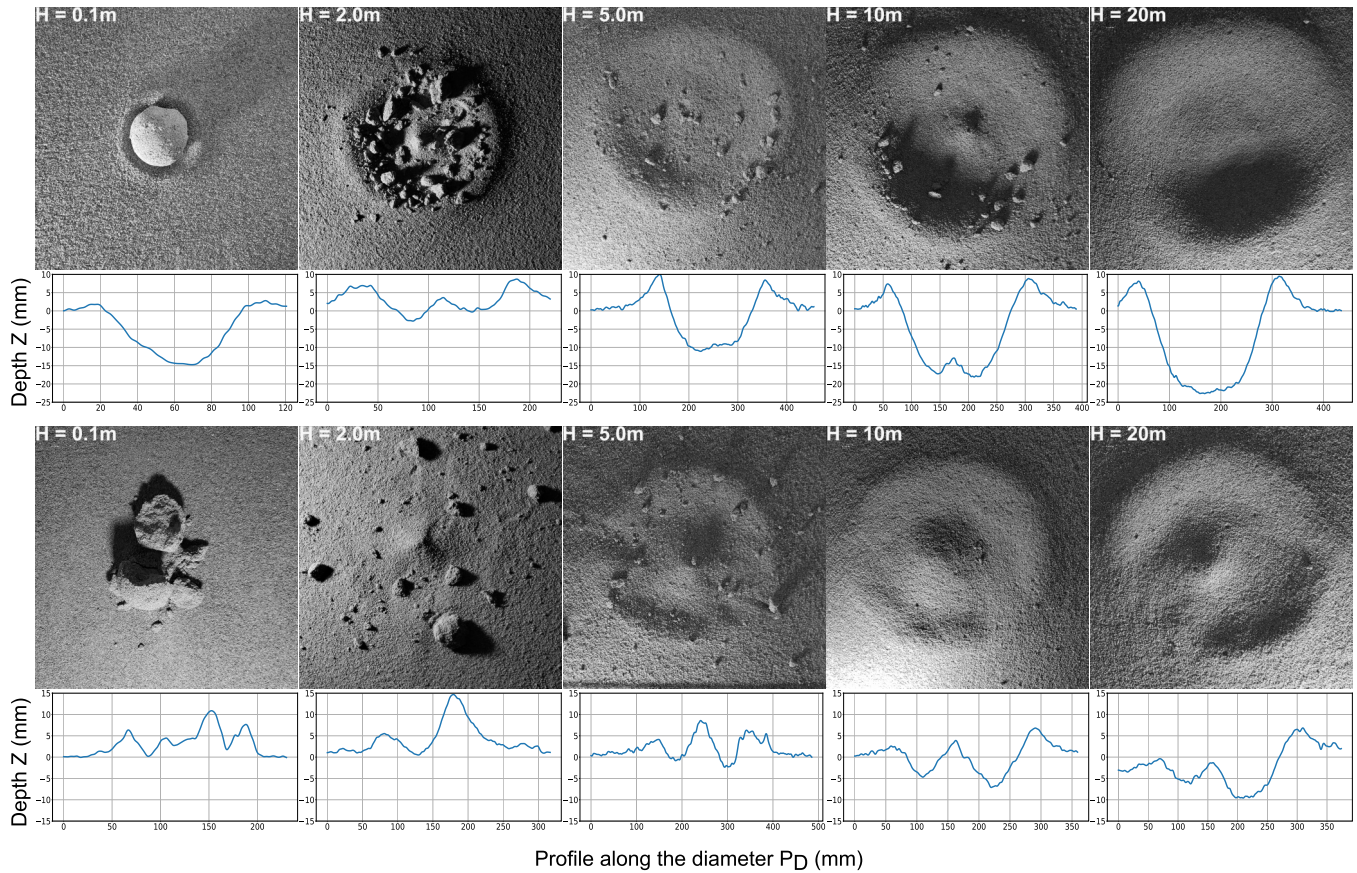


FIG. 1. Subsequent pictures of the crater formed by the impact of granular projectiles at different heights. At the bottom of each image, depth profiles along the diameter obtained with the CRATERSLAB library are added. First row corresponds to a loose-packed sand bed and second row corresponds to a compacted sand bed.

mound on top of the target terrain and it is surrounded by scattered projectile fragments; see Figs. 1 and 2(a) in [8]. A clearly distinguishable crater is not formed until the collision excavates below the ground surface. Therefore, we consider a circular region containing most (approximately 90 percent) of the remaining mound material by searching the limits at which the terrain does not present further elevation with respect to the ground level. The diameter of this region is defined as the diameter of the mound. These mounds will be represented with triangular symbols in our plots.

These mounds are the precursors to the central peaks that will appear in excavated craters once the energy overpasses the threshold required for which the impact excavates below the ground surface. The larger fragments (representing less than approximately 1/20 part of the projectile diameter) that are not considered part of the mound progressively decrease in size and scatter further away from the impact point as the dropping energy increases. The crater begins to exhibit a subtle rim and a central peak increasing its depth as the energy grows. At sufficiently high energies, the crater appears to replicate the growth process observed in loosely packed sand craters, but with smaller diameters and depths.

The complex craters obtained in experiments with granular impactors against granular surfaces are flat, like tortillas, with tall central peaks. Every crater formed on compacted targets has a central peak, while a few, randomly distributed craters

formed on loosely packed targets lack this feature, as can be seen in Fig. 1 and marked as hollow symbols in other figures.

A. Diameter

Let us now analyze the growth of the crater diameter (D) as a function of impact energy. Uehara and co-workers [14] reports that the crater diameter scales with an exponent of 1/4 concerning the projectile’s impact energy as a universal law, as shown in Eq. (1). This result is observed for craters formed by solid balls dropped into dry, noncohesive, granular media, where the ball’s density ρ_b , its diameter D_b , and the dropping height H are varied. The employed model is based on a “gravity-limited” regime, where the energy is primarily utilized to lift a volume of $\sim D^3$ to a height of $\sim D$ against the force of gravity,

$$D = 0.92[\rho_b/(\rho_g\mu^2)]^{1/4}D_b^{3/4}H^{1/4}. \tag{1}$$

Additionally, Pacheco and colleagues [8] made experiments similar to those conducted by Uehara while using granular projectiles with varying porosity and keeping their diameter constant. Interestingly, certain similarities were observed with crater morphologies produced by solid spheres since both obey the scaling law proposed by Uehara for the crater diameter. However, Pacheco *et al.* extended the Uehara law for diameter versus energy to describe the appearance of

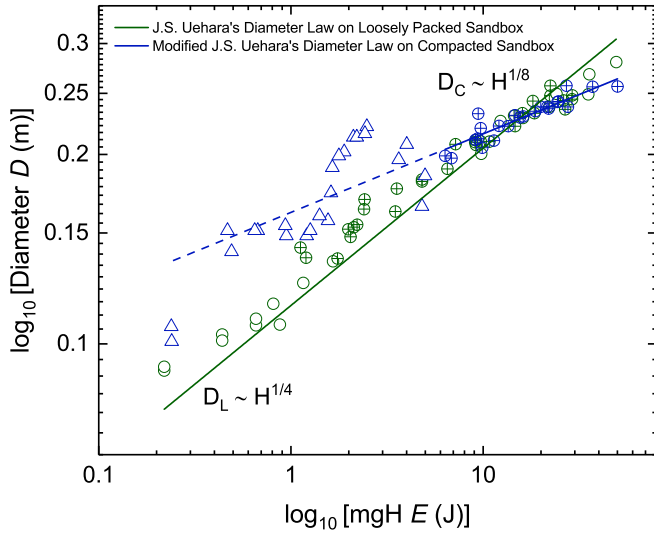


FIG. 2. Uehara’s law for diameter growth as a function of impact energy in experiments on loosely packed and compacted sandbox targets. The symbols represent Δ sand mounds, \circ simple crater formation, and \oplus complex crater formation.

a gap between the diameters, employing Eq. (2),

$$D = C[\rho_b/(\rho_g)]^{1/4} D_b^{3/4} H^{1/4} + (\Delta D)\Theta(H - H_f). \quad (2)$$

Figure 2 represents the diameter as a function of energy for our experiments in loosely or compacted packed sandbox targets. In no case did we observe a gap between the diameters described in Eq. (2). For this reason, we proceed to fit the data using the Uehara equation for diameter [Eq. (1)] with the static friction coefficient μ as a free parameter. The rest, including the density and diameter of the impactor and the density of the granular medium, were fixed to our experimental data. In the case of loosely packed sand, Eq. (1) fits well, and a slope angle ($\arctan \mu = \theta$) is obtained for the free parameter of $\theta = 40.2^\circ$, which aligns with the angle of repose of our granular medium.

However, when applying the same procedure to the data from compacted sandbox targets, we found that Eq. (1) does not accurately fit with a coefficient of determination (COD) or a R -squared value of $R^2 = 0.082$. Nevertheless, by modifying one of its exponents to the form $D \sim H^{1/8}$, the fit improves significantly. This exponent is suggested by the best fit of the data. By making this modification to Eq. (1) and fitting it to the data, we achieve a good fit ($R^2 = 0.82$) but a low angle of repose of $\theta = 23.2^\circ$, which does not correspond to the angle of repose of our granular medium.

In the fitting process for this experimental group, the data from sand mounds are not considered since they do not correspond to crater formation due to the absence of penetration into the impact surface. Nonetheless, their diameters are determined based on our criteria and included in Fig. 2 because a gradual growth is observed. This diameter increase can be associated with the energy required to reach a critical level that allows excavation on the surface for crater formation. Ultimately, their gradual growth before and after surpassing the yield strength of the surface is interesting.

It can be asserted that the dependence of the diameter on impact energy for a loosely packed surface adheres to

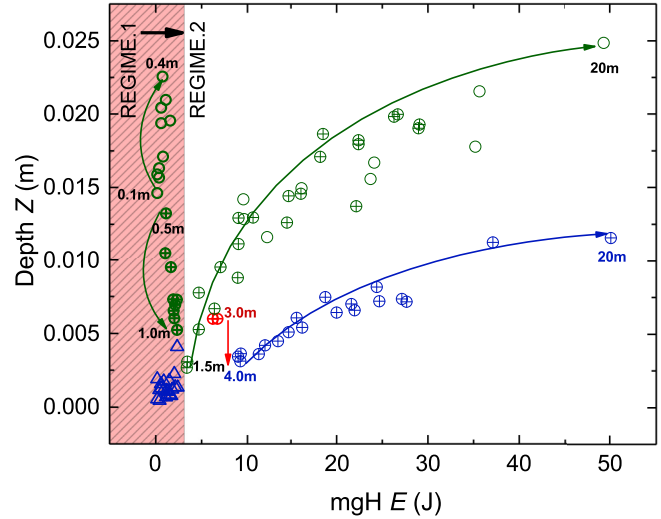


FIG. 3. The transition between depth regimes in crater formation for loosely and compacted sandbox targets. The symbols inside the red area correspond to the first regime. In the second regime, the symbols \oplus belong to experiments on compacted sandbox targets, but are excluded from the data because they represent data from the first regime (at a height of 3.0 m), although they are not located within the red area. The arrows represent a visual guide of the evolution of depth while varying the dropping height for both experimental sets.

Uehara’s law because it follows the volume displacement model for a gravity-limited regime. However, for a compacted surface, even though it still exhibits a power-law relationship, this regime undergoes a notorious change in the exponent, showing a still unknown underlying physical mechanism preventing the diameter from increasing in the same manner.

B. Depth

Since the crater’s depth is the central issue of this research, we plotted the maximal depth of excavated craters as a function of energy in which we found two regimes. This abrupt transition between depth regimes is characterized by differing behaviors (see Fig. 3), with our emphasis on the second regime. The first regime occurs at lower dropping heights for both loosely (from 0.1 to 1.0 m) and compacted (from 0.1 to 3.0 m) sandbox targets, respectively, while the second regime takes place at higher dropping heights.

This transition from one regime to the other stands for the fragmentation of the projectile as the dynamic pressure of the projectile at impact overcomes its own yield stress. The comminuted material deposits, partially filling the just opened crater, and thus produces a nonmonotonic behavior of the depth as a function of dropping energy. In the same Fig. 3, the first regime in which the projectile has preserved integrity, or at least part of it, is remarked with a reddish color. From here on, it is important to note that data in some graphs represent only a fraction of the complete dataset due to the observation of these different regimes, and we will mainly focus on the regime after the fragmentation transition that was just described has overcome.

We examine the depth’s dependence on impact energy (see Fig. 4), in light of the Uehara model, which also defines a

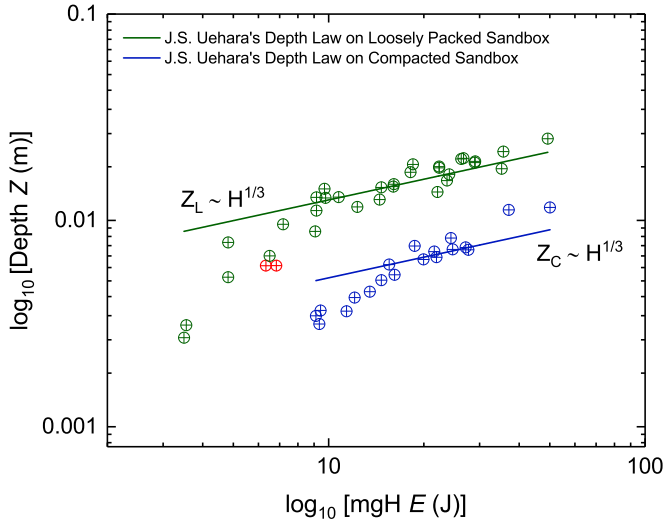


FIG. 4. Uehara's law for depth growth as a function of impact energy. The symbols represent \circ simple crater formation, \oplus complex crater formation, and \otimes excluded data points from experiments on a compacted sandbox target, which are part of the first depth regime.

universal law for the depth of the crater vs impacting energy, given by

$$Z = 0.16[\rho_b/(\rho_g\mu^2)]^{1/2}D_b^{2/3}H^{1/3}. \quad (3)$$

One gets the results shown in Fig. 4, where we performed a fit using Eq. (3), with the static friction coefficient as a free parameter following the same procedure as was employed in the diameter fitting, in this case, $\arctan \mu = \theta$. Clearly, as observed, the Uehara model for depth as a function of impact energy poorly fits our experiments on both loosely and compacted sandbox targets, and the values of our free parameter deviate significantly ($\theta = 73.1^\circ$ on loosely packed sand and $\theta = 82.8^\circ$ on compacted sand) from the real friction coefficient that is measured. Figure 4 does not adhere to a power-law relationship, and the Uehara model is not capable of describing the growth of depth with impacting energy.

Based on observations of granular impactors against granular impact surfaces, such as the experiments in two dimensions (2D) performed by Bartali *et al.* [13], in which the crumbled or pulverized projectile acts more like a piston compressing the target's terrain, we can observe that the depression forming the crater's bottom is caused by subsidence of the free surface of the target due to the compressive stress exerted by the projectile impact.

Following the mechanism revealed by these 2D experiments, we propose a uniaxial compaction process occurring vertically in order to explain the depth-energy relationship, a mechanism which does not align with the volume displacement model from which Eq. (3) was derived.

In order to explain the depth vs energy dependence, we propose a compaction model based on Heckel's law [15], commonly used in the pharmaceutical industry [16], where a solid piston compacts a granular medium. However, in our case, we would be dealing with a porous piston made of sand, which is part of the pulverized granular projectile. Thus, according to Heckel's law, the compressibility of our granular

sandbox target will be proportional to its porosity. Therefore, the available space for compaction can be expressed as

$$\frac{d\phi}{dP} = K(\phi_{\max} - \phi), \quad (4)$$

where ϕ is the volume fraction of the target, P is the pressure, K is a constant, and ϕ_{\max} is the maximum packing fraction of the granular medium. By integrating Eq. (4), it transforms into

$$\phi = \phi_{\max} - (\phi_{\max} - \phi_0) \exp^{-K(P-P_0)}, \quad (5)$$

where K is a free parameter, which we will refer to as the compacting susceptibility of the granular medium, ϕ_0 is the packing fraction of the medium before experiencing uniaxial compressive stress, ϕ_{\max} is the maximum packing fraction that the medium reaches when subjected to vertical dynamic pressure P , and P_0 is the initial dynamic pressure, which in our case corresponds to the pressure the medium experiences when the projectile hits the target $P_0 = \rho v^2/2$, with v the impact velocity and ρ the projectile's density.

In order to corroborate Eq. (5), we will transform the axes of Fig. 4 from depth Z to packing fraction ϕ and from energy E to the dynamic pressure P applied to the target.

First, we define the packing fraction (ϕ). This parameter characterizes the spatial arrangement of granular ensembles and is expressed as the ratio of the volume occupied solely by the grains to the total volume encompassed by the ensemble, accounting for the interstitial voids among individual grains. An alternative formulation of the packing fraction involves the quotient of the density of the granular ensemble (ρ_{GP}) divided by the density of the solid material (ρ_s) composing the grains, expressed as $\phi = \rho_{GP}/\rho_s$.

For a vertical cylindrical container with a cross-sectional area A and height h , filled to its rim with granular material, we define its density ρ_0 . This density corresponds to the initial density of the ensemble before impact, denoted either as ρ_L for a loosely packed medium or ρ_C for a compacted one. ρ_0 is determined by dividing the mass m of the granular material by the product of the cross-sectional area and the height, $A \cdot h$.

Subsequently, if we uniformly compress the granulate along its vertical axis by a distance Z , while maintaining the transverse section, we achieve a granular packing with a new density given by $\rho_{GP}(Z) = m/A(h - Z)$. However, it is important to note that we are simplifying by assuming uniform compaction throughout the granulate. In reality, compressive stress induces a density gradient within the granular material [17].

The quotient of these two densities is expressed as

$$\frac{\rho_{GP}(Z)}{\rho_0} = \frac{h}{h - Z}. \quad (6)$$

Finally, from the second definition of the packing fraction and Eq. (6), we obtain

$$\phi(Z) = \frac{\rho_0}{\rho_s} \frac{h}{h - Z}. \quad (7)$$

It can be noted that Z acquires its maximum allowed value when the density of the granular ensemble reaches the closest packing achievable. Since we are dealing with nondeformable grains, the final packing fraction would be a complex function of the shape and size distribution of grains. For example, a

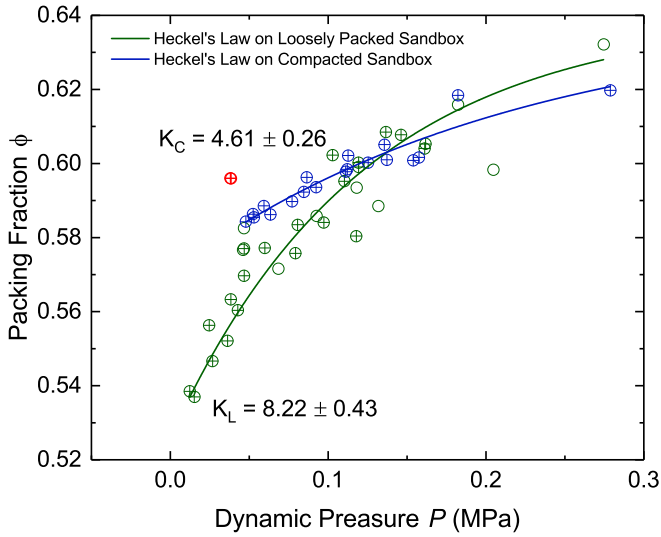


FIG. 5. Heckel compaction model for both loosely packed and compacted targets. The symbols \oplus represent excluded data points from experiments on a compacted target, which are part of the first energy vs depth regime.

set of randomly packed, identical spheres would achieve a volume fraction of 0.64, while for a perfectly ordered array of identical hard spheres, it will reach 0.74.

On the other hand, the impact energy per unit volume is essentially the dynamic pressure, denoted as $P = \rho gH$. This concept can be likened to the pressure exerted by a vertical water (sand) jet striking the sandbox target, where the area in which momentum is transferred is considered as the constant transversal section of our projectile.

By using Eq. (7) to transform our values of depth Z into volume fractions ϕ , and using the relationship of dynamic pressure as a function of the energy to plot ϕ vs P , Fig. 4 gives rise to Fig. 5, displaying the fit of Eq. (5) for the second regime for both loosely packed and compacted sandbox targets, each with its respective free parameters K_L and K_C .

The Heckel-based model elucidates the saturation of depth through a compaction mechanism, tending to a filling fraction equal to random close packing, $\phi_{RCP} = 0.64$ [18], employing an exponential law. The compacting susceptibilities K_L and K_C offer insights into the medium's easiness of compacting as the dynamic pressure increases. In this context, K_L is nearly twice that of K_C .

On the other hand, the primary reason for these differing susceptibilities, i.e., K_L and K_C , is better explained by the

way in which projectile fragments are more easily expelled horizontally with the ejecta for compacted targets compared to loosely packed ones. This phenomenon was observed during experiments where the ejected material was thrown away from the impact zone much faster in compacted targets than in loosely packed targets for the same impacting energy, as can be seen in Fig. 6. Consult the Supplemental Material [19] to observe the increase in vertical-to-horizontal momentum transfer as the impact surface compacts.

To verify this phenomenon, side-view videos of the impact zone were captured at 960 frames per second (fps) and the velocities of the material ejection and the displacement of the crater opening ejecta crown were measured. Upon conducting an analysis of these videos, it was determined that an ejection angle with respect to the horizontal angle of 45° for loosely packed targets, a 30° angle for compacted targets, and less than 10° angle for a solid target corroborates larger vertical to horizontal coefficients of momentum transfer for compacted versus loosely packed targets. In addition, a horizontal speed of the ejecta of 3.63, 5.20, and 10.56 m/s for loosely, compacted, and solid targets, respectively, was measured.

Let us now make an analysis using a simple energy balance for assessing the energy spent in opening the craters in each case.

Assume the effective stopping force F_r as constant during the subsidence of the crater's floor, and the fraction of energy transferred from vertical to horizontal $\kappa_{vh}mgH$, where κ_{vh} stands for a transferred coefficient of vertical to horizontal momentum; thus, the conservation of energy must satisfy

$$\kappa_{vh}mgH + \int_0^Z F_r dl = mgH. \quad (8)$$

This is simply the work done by the frictional force plus the energy of the ejected material as a function of impact energy. We can assume that the frictional force is a drag force proportional to the area of the crater's floor, $F_r \propto \mu_e A_c \propto \mu_e D^2$, where μ_e is the effective friction coefficient of the packing and A_c is the area of the crater's floor. Therefore, Eq. (8) transforms into

$$D^2 Z \propto \frac{1 - \kappa_{vh}}{\mu_e} mgH. \quad (9)$$

Figure 7 shows the energy balance approximation. It can be observed that the slope of the loosely packed experiments (in green) is nearly three times the slope for compacted experiments.

However, considering that the effective friction coefficient tends to increase as the density of the granular packing

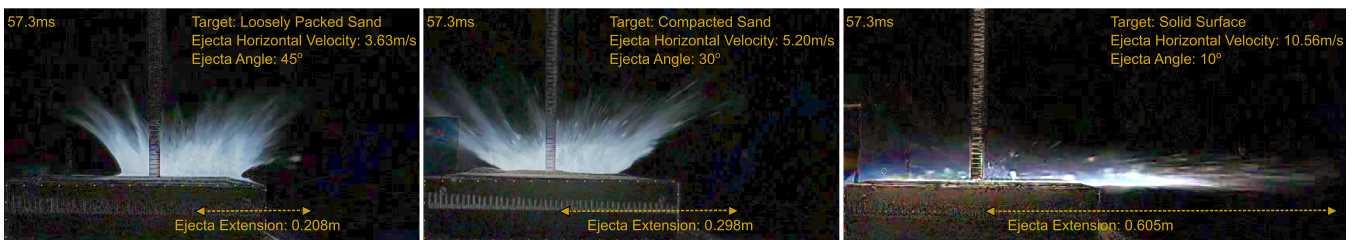


FIG. 6. From left to right, differential images of the ejecta taken at 57.3 ms after first impact for loosely packed, compactly packed, and solid targets, respectively.

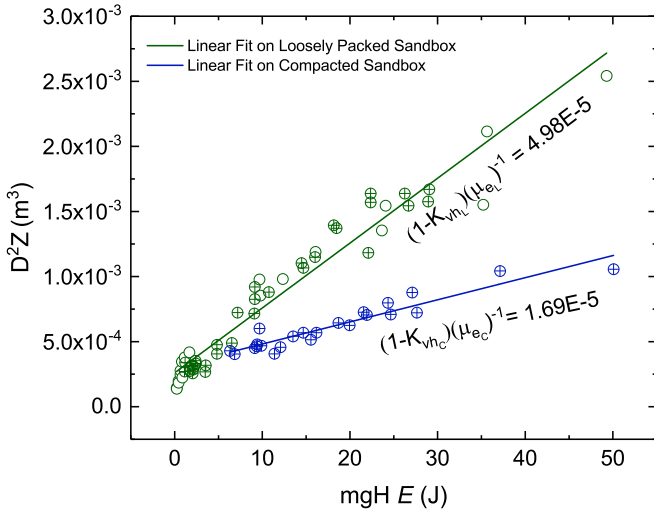


FIG. 7. Energy balance between stopping forces proportional to D^2Z in relation to the impact energy. The vertical momentum transfer to horizontal is higher for compacted sandbox targets.

increases due to grains tending to be more closely packed [20], the effective friction coefficients can be expressed proportionally to their respective densities of the loosely packed and compacted sand media as follows: $\mu_{eL} \propto \rho_L = 1.39 \text{ g/cm}^3$ and $\mu_{eC} \propto \rho_C = 1.52 \text{ g/cm}^3$. In this way, we can resolve the slopes of Fig. 7 and it can be deduced that $\kappa_{vhC} > \kappa_{vhL}$.

This result remains consistent with compaction susceptibility determinations, where their differences are attributed to the mechanism of greater transfer of vertical momentum to horizontal momentum in a compacted sandbox compared to a loosely packed sandbox. The energy balance not only confirms this more efficient transfer mechanism, but also offers a physical model to understand the crater formation process.

Upon impact, several processes unfold. The projectile first penetrates the target until the dynamic pressure reaches its yield stress, resulting in fragmentation and the formation of a “porous piston” made of pulverized sand. This porous piston exerts pressure on the receding target surface, while stresses propagate downward, compacting the target material producing subsidence of the crater’s floor and establishing a compaction gradient below [17]. Simultaneously, a central mound or peak develops, which is the lower part of the projectile trapped between the crater’s floor and the rest of the projectile flowing downward due to dynamic pressure [21].

We consider that friction plays a significant role in the compaction processes of both loosely and tightly packed sandbox targets [22], but we still lack a clear understanding of its relationship with compacting susceptibility. We acknowledge that there are distinctions between the macroscopic mechanisms that we describe and the actual microscale processes [23] that lead to the effective friction coefficient that we utilize.

In our experiments with compacted sand, we observe shallower craters with lower rims and smaller diameters compared to those formed in loosely compacted targets. The projectile hardly excavates below the ground surface, and a larger mound or central peak is more easily formed, in comparison to loosely packed targets, peaks that likely promote a better verti-

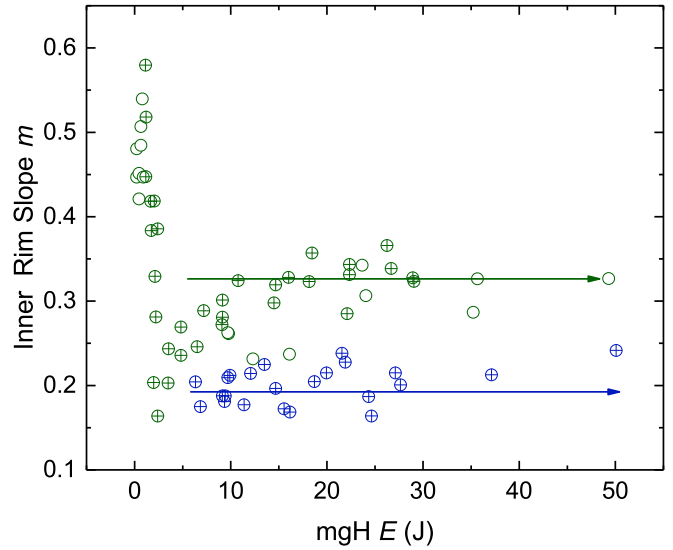


FIG. 8. Interior slopes of the crater rim for both loosely packed and compacted sandboxes. In both cases, the saturation of the interior slopes is noticeable. Craters in the compacted sandbox exhibit flatter profiles with lower interior slopes compared to those in the experiments conducted in the loosely packed sandbox. The arrows serve as a visual guide to highlight the saturation of the inner slopes in both experimental groups.

cal to horizontal transfer of momentum: these two phenomena makes smother inner rim slopes (see Fig. 8), precluding further radial growth of the crater (smaller diameters than in loosely packed targets for the same energy). Further investigation is warranted to elucidate the mechanism underlying the increased backscattering of ejecta from loosely packed targets compared to more densely compacted or solid targets.

As a remark, let us say that the Uehara model describes a different physical system than our experiments in the sense that for solid vs granular collisions, there is no compaction of the target in the vertical direction, but instead a penetration of a solid into a dense gas of solid particles followed by evacuation of a certain amount of material. In contrast, for fragile softly consolidated aggregates of sand, the projectile crumbles into small fragments upon the impact and spreads over a larger area than the projectile’s cross section, pressing down and causing a compressive subsidence of the target’s terrain. Thus it is natural that the Uehara’s model does not accurately describe the vertical excavation of our experiments.

However, in granular collisions, part of the energy is diverted towards horizontal degrees of freedom in the same way as the displaced material from a solid vs granular collision, and some correspondence can be expected among granular lumps vs granular targets and solid vs granular target craters for the predicted diameter. This horizontally diverted material produces the ejecta and contributes to the formation of the crater’s rims.

C. Aspect ratio

Finally, we analyze the depth aspect ratios as a function of the diameter in our experiments and compare them with the aspect ratios of lunar craters obtained through direct ob-

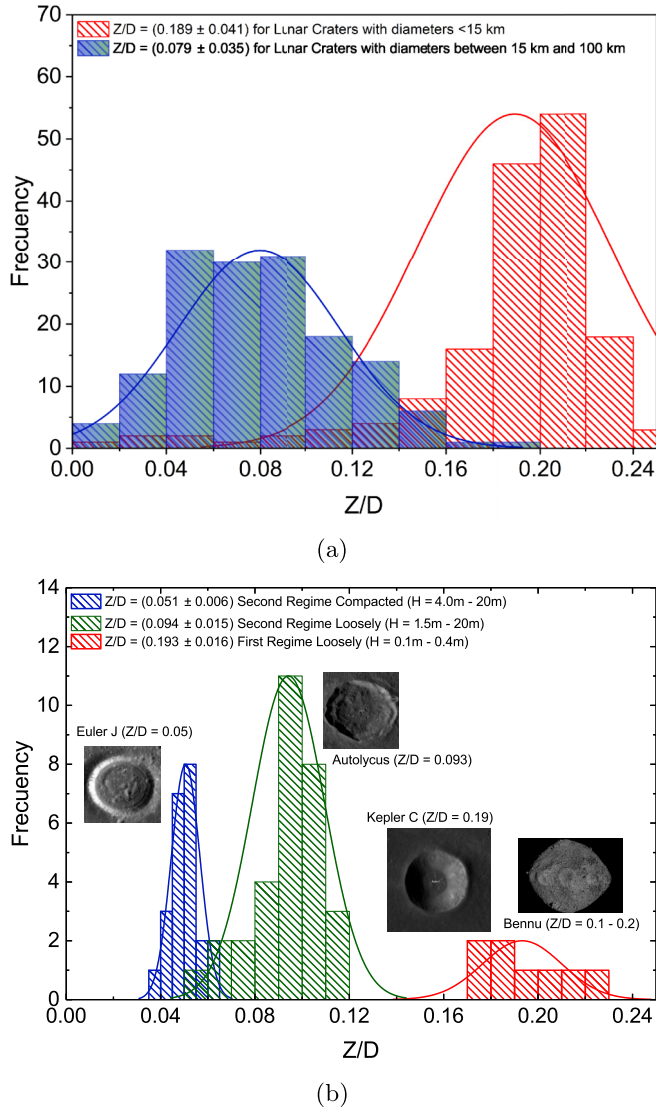


FIG. 9. Aspect ratio between diameter and depth. (a) Aspect ratios directly measured from observational values. The blue-green distribution corresponds to craters with diameters between 15 and 100 km, while the second red distribution represents the aspect ratio for craters with diameters below 15 km. (b) Experimental aspect ratios for both loosely packed and compacted sandbox scenarios. The initial blue distribution corresponds to dropping heights of 4.0–20 m in the compacted sandbox. The subsequent green and red distributions correspond to the loosely packed sandbox for dropping heights of 1.5–20 m and 0.1–0.4 m, respectively.

servational measurements conducted on more than 300 lunar craters; see Fig. 9. The purpose of this comparison is to interpret the shallowness of planetary craters in the context of the uniaxial compression mechanism proposed in this study. It is noteworthy that the depth utilized to calculate the aspect ratio aligns with the commonly employed measurement in the astronomical scientific community, extending from the height of the crater rim to the point of maximum depression within.

In our experiments, we will focus on the case of loosely packed sand, specifically on the aspect ratios between drop-

ping heights of 0.1–0.4 m and 1.5–20 m. The data between dropping heights of 0.5 and 1 m contain a significant portion of impactor remnants; for this reason, they are not considered for analysis. In compacted sandbox experiments, we will continue to focus on the second regime because, in the first regime, the impact energies do not exceed the yield strength of the impact surface and there is no visible penetration into it.

The aspect ratio determined in the experiments conducted in the loosely packed sandbox for dropping heights between 0.1 and 0.4 m [red distribution in Fig. 9(b), $Z_L = (0.193 \pm 0.016)D_L$] closely aligns with the aspect ratio observed in lunar craters with diameters below 15 km [red distribution to the right in Fig. 9(a)]. This particular aspect ratio corresponds to simple crater-bowl-shaped depressions with raised rims and approximately parabolic interior profiles, with diameters smaller than 15 km, exemplified by the lunar crater Kepler C [24]. Additionally, during the OSIRIS-REx spacecraft’s mission to the asteroid Bennu in 2020, craters of a few meters in diameter were discovered with aspect ratios ranging between 0.1 and 0.2 [25].

In contrast, experimentally, for higher impact energies, aspect ratios of $Z_C = (0.051 \pm 0.006)D_C$ and $Z_L = (0.094 \pm 0.015)D_L$ are observed [blue and green distributions in Fig. 9(b)]. These align with many of the aspect ratios of lunar craters with diameters between 15 and 100 km, as evident in the blue-green distribution in Fig. 9(a). This category includes lunar craters with flat interiors and larger diameters, such as crater Autolykus [26] and crater Euler J [27].

The striking similarity between observational and experimental aspect ratios deepens our insight into the planarity of lunar craters, allowing us to interpret it through the proposed uniaxial compression model. This contribution significantly advances our understanding of crater morphogenesis.

IV. CONCLUSIONS

In summary, impact crater experiments were conducted, varying the compaction of the sandbox target. The power-law relationship governing crater diameters exhibited consistency with a volume-displacement model for experiments conducted on loosely packed sand, while a more favorable fit with an exponent of $\sim 1/8$ was obtained for the compacted sandbox target. This new exponent, even though it still exhibits a power-law relationship, indicates an underlying physical mechanism that prevents the diameter from increasing in the same manner, which remains unknown. Conversely, the power-law model for volume displacement did not yield a satisfactory depth fit in either case.

To address this limitation, we introduce a uniaxial compression model with an exponential law that explains how depth saturates to a filling fraction equal to random close packing. This model elucidates the underlying physical mechanisms of vertical compression and lateral excavation of the crater and the transfer of momentum between these degrees of freedom. Planetary craters were found to be more likely formed by granular impacts on granular surfaces, underscoring the paramount importance of understanding the crater-opening mechanisms in such collisions. Therefore, the

proposed model represents an alternative theoretical tool for addressing this longstanding problem. Within this energy balance framework, frictional forces play a pivotal, but not revealed role.

Our results reveal a greater transfer of vertical to horizontal momentum on compacted surfaces compared to loosely packed sandbox targets. Furthermore, our findings indicate that the depth-to-diameter aspect ratio results are consistent with prior and current observational data from planetary

bodies, providing significant insights into the physical processes governing natural crater formation.

ACKNOWLEDGMENTS

We would like to express our sincere gratitude to Dr. E. Altshuler for his invaluable assistance in preparing this manuscript. F.C.-M. acknowledges the CONAHCYT scholarship with Grant No. CVU 1050049.

-
- [1] E. Richardson, The impact of a solid on a liquid surface, *Proc. Phys. Soc.* **61**, 352 (1948).
- [2] M. E. Center, High-speed photography techniques (unpublished), <https://edgerton.mit.edu/>.
- [3] F. Pacheco-Vázquez, Ray systems and craters generated by the impact of nonspherical projectiles, *Phys. Rev. Lett.* **122**, 164501 (2019).
- [4] V. Inglezakis, Extraterrestrial environment, in *Environment and Development*, edited by S. G. Pouloupoulos and V. J. Inglezakis (Elsevier, Amsterdam, 2016), pp. 453–498.
- [5] Y. Tsuda, M. Yoshikawa, T. Saiki, S. Nakazawa, and S.-i. Watanabe, Hayabusa2–Sample return and kinetic impact mission to near-earth asteroid Ryugu, *Acta Astronaut.* **156**, 387 (2019).
- [6] H. J. Melosh, *Impact Cratering: A Geologic Process* (Oxford University Press/Clarendon Press, New York, 1989).
- [7] G. K. Gilbert, The Moon's face: A study of the origin of its features, in *A Source Book in Astronomy and Astrophysics* (Harvard University Press, Cambridge, Massachusetts, 1979), pp. 80–87.
- [8] F. Pacheco-Vázquez and J. C. Ruiz-Suárez, Impact craters in granular media: Grains against grains, *Phys. Rev. Lett.* **107**, 218001 (2011).
- [9] J. R. Royer, E. I. Corwin, A. Fiori, M.-L. Cordero, M. L. Rivers, P. J. Eng, and H. M. Jaeger, Formation of granular jets observed by high-speed x-ray radiography, *Nat. Phys.* **1**, 164 (2005).
- [10] R. Bartali, G. M. Rodríguez-Liñán, Y. Nahmad-Molinari, D. Sarocchi, and J. C. Ruiz-Suárez, Role of the granular nature of meteoritic projectiles in impact crater morphogenesis, [arXiv:1302.0259](https://arxiv.org/abs/1302.0259).
- [11] G. Viera-López and F. Corrales-Machín, Craterslab (2023), <https://github.com/gvialopez/craterslab>.
- [12] F. Corrales-Machín, G. Viera-López, R. Bartali, and Y. Nahmad-Molinari, Morphological study of granular-granular impact craters through time-of-flight cameras: from concept to automation in PYTHON, [arXiv:2310.13834](https://arxiv.org/abs/2310.13834).
- [13] R. Bartali, Y. Nahmad-Molinari, and G. M. Rodríguez-Liñán, Low speed granular-granular impact crater opening mechanism in 2D experiments, *Earth Moon Planets* **116**, 115 (2015).
- [14] J. S. Uehara, M. A. Ambroso, R. P. Ojha, and D. J. Durian, Low-speed impact craters in loose granular media, *Phys. Rev. Lett.* **90**, 194301 (2003).
- [15] R. W. Heckel, Density-pressure relationships in powder compaction, *Trans. Metal. Soc. AIME* **221**, 671 (1961).
- [16] I. Klevan, J. Nordström, A. Bauer-Brandl, and G. Alderborn, On the physical interpretation of the initial bending of a Shapiro-Konopicky-Heckel compression profile, *Eur. J. Pharmaceut. Biopharmaceut.* **71**, 395 (2009).
- [17] M. Hajjalilue-Bonab and A. Rezaei, Physical modelling of low-energy dynamic compaction, *Intl. J. Phys. Model. Geotech.* **9**, 21 (2009).
- [18] B. Andreotti, Y. Forterre, and O. Pouliquen, *Granular Media: Between Fluid and Solid* (Cambridge University Press, Cambridge, 2013).
- [19] See Supplemental Material at <http://link.aps.org/supplemental/10.1103/PhysRevE.109.054907> for detail the transition from vertical to horizontal momentum. It can be observed that there is a greater transfer of momentum as the impact surface becomes more compact.
- [20] F. Zhou, S. G. Advani, and E. D. Wetzel, Slow drag in granular materials under high pressure, *Phys. Rev. E* **69**, 061306 (2004).
- [21] Y. Amarouchene, J. F. Boudet, and H. Kellay, Dynamic sand dunes, *Phys. Rev. Lett.* **86**, 4286 (2001).
- [22] J. Duran, *Sands, Powders, and Grains: An Introduction to the Physics of Granular Materials* (Springer Science & Business Media, New York, 2012).
- [23] M. Cárdenas-Barrantes, D. Cantor, J. Barés, M. Renouf, and E. Azéma, Micromechanical description of the compaction of soft pentagon assemblies, *Phys. Rev. E* **103**, 062902 (2021).
- [24] Lunar QuickMap, Kepler C (2024), <https://bit.ly/49h1SeN>. We acknowledge the use of imagery from Lunar QuickMap (<https://quickmap.lroc.asu.edu>), a collaboration between NASA, Arizona State University, and Applied Coherent Technology Corp.
- [25] R. T. Daly, O. S. Barnouin, E. B. Bierhaus, M. G. Daly, J. A. Seabrook, R. L. Ballouz, H. Nair, R. C. Espiritu, E. R. Jawin, D. Trang *et al.*, The morphometry of small impact craters on Bennu: Relationships to geologic units, boulders, and impact armoring, *Icarus* **384**, 115058 (2022).
- [26] Lunar QuickMap, Autolyus (2024), <https://bit.ly/3Sm6dXp>. We acknowledge the use of imagery from Lunar QuickMap (<https://quickmap.lroc.asu.edu>), a collaboration between NASA, Arizona State University, and Applied Coherent Technology Corp.
- [27] Lunar QuickMap, Euler J (2024), <https://bit.ly/4bjf0lq>. We acknowledge the use of imagery from Lunar QuickMap (<https://quickmap.lroc.asu.edu>), a collaboration between NASA, Arizona State University, and Applied Coherent Technology Corp.